Hindawi
Geofluids
Volume 2021, Article ID 6664882, 13 pages
https://doi.org/10.1155/2021/6664882

Research Article

A Dynamic Cavity Expansion Model for Rigid Projectile Penetration into Concrete considering the Compressibility and Nonlinear Constitutive Relations

Fei Gao, Zhen Wang, Zhu Wen, and Yuguo Ji

School of Mechanical Engineering, Nanjing University of Science and Technology, Nanjing 210094, China

Correspondence should be addressed to Zhen Wang; wangzhen2012@njust.edu.cn

Received 11 November 2020; Revised 7 December 2020; Accepted 23 December 2020; Published 6 January 2021

Academic Editor: Zhigang Tao

The P-α equation of state (EOS) and a nonlinear yield criterion are utilized to characterize the dynamic constitutive behavior of concrete targets subjected to projectile normal penetration. A dynamic cavity expansion model considering the compressibility and nonlinear constitutive relations for concrete material is developed. Then, a theoretical model to calculate the depth of penetration (DOP) for rigid projectile is established. Furthermore, the proposed model is validated based on the available test data as well as the calculation results by the linear compressible EOS and linear yield criterion. This study shows that the proposed model derived using the P-α EOS and nonlinear yield criterion can effectively reflect the plastic mechanical properties of concrete and is also suitable for predicting the DOP of concrete targets. In addition, the influence law of concrete constitutive parameters such as the cohesion strength, shear strength, internal friction coefficient, and elastic limit pressure on the DOP is revealed.

1. Introduction

The dynamic response and destruction of concrete structures under explosive or impact loading have important theoretical and application value in the field of weapon damage and engineering protection [1]. Li et al. [2] systematically reviewed the empirical formulas, theoretical analyses, and numerical methods related to the concrete penetration problem. To evaluate the damage and failure behavior of concrete, a large number of penetration tests [3–8] have been conducted. The penetration process is driven not only by the mortar strength, aggregate size, aggregate sliding, and redistribution behavior but also by pore breakage and compaction. Therefore, the compressibility and nonlinear effect of concrete must be considered in the process of theoretical analysis.

Cavity expansion theory is an accepted analytical method for studying the penetration mechanism of projectiles into a target. Bishop et al. [9] proposed quasi-static cylindrical and spherical cavity expansion equations in a semi-infinite target. Hill [10] modified a spherically symmetric dynamic cavity expansion equation for an incompressible medium. To date, the cavity expansion model is widely used to evaluate the penetration resistance of projectiles into concrete [11–17], rock [18–20], ceramics [21, 22], sand [23, 24], soil [25], and metal [26, 27] targets. When the appropriate EOS and yield criterion are adopted, the numerical and analytical solution for the model will be solved by the similarity transformation method.

In the current works that focus on reducing the complexity in the cavity expansion analysis, the simplified EOS is usually used such as incompressible [12], linearly compressible [12, 22], and locked hydrostatic [11, 13] models. Although the incompressibility hypothesis can reduce the difficulty of the analysis step, the DOP obtained by the incompressible EOS is much shallower than the corresponding test data [12]. The linearly compressible model is approximately available for the case of low striking velocities. Therefore, neither the linear model nor the locked model can accurately reflect the compression process of concrete.

After reviewing the yield criteria, it was found that the original and revised forms of the Tresca [11], Mohr-Coulomb [12, 14, 19, 22–24], and Drucker-Prager [15] models have been widely used in dynamic cavity expansion analyses for concrete-like material. However, all the above-mentioned yield criteria are in linear form. When considering the triaxial shear data in the present paper, the results show that the relationship between the pressure and shear strength is nonlinear, especially under high pressure. In summary, a model considering pore compaction, a nonlinear EOS, and nonlinear yield criterion are needed to calculate the DOP of projectiles into concrete targets.

This paper proposes a P-α EOS and nonlinear yield criterion for rigid projectiles penetrating concrete targets on the basis of a comparative analysis of existing concrete constitutive models. A spherical cavity expansion model considering the compressibility and nonlinear constitutive relations of concrete is established, and the cavity pressure is calculated. Furthermore, the calculation model for the DOP is derived, and the validity of the model is demonstrated by a comparison with the results of the widely recognized model as well as the available penetration test data [12]. Eventually, the influences of the constitutive parameters on the DOP are discussed.

2. Constitutive Model

In the following section, the hydrostatic behavior and strength model for concrete are treated separately and described by the P-α EOS and nonlinear yield criterion, respectively.

2.1. Equation of State. The concrete exhibits pore compaction and permanent densification effect when subjected to high-pressure loading [28]. The P-α EOS originally proposed by Herrmann [29] can be used to describe the compressibility of concrete. The P-α EOS for concrete can be expressed by Eq. (1).

$$\alpha = \begin{cases} \alpha_0 & P \le P_e \\ 1 + (\alpha_0 - 1)\left(\dfrac{P_s - P}{P_s - P_e}\right)^3 & P_e < P \le P_s \\ 1 & P > P_s \end{cases}, \tag{1a}$$

$$\alpha = \frac{\rho_s}{\rho} \ge 1, \tag{1b}$$

where α and α_0 are the porosities of the current and initial material, respectively; ρ and ρ_s are the densities of the current and fully compacted material, respectively; P is the current pressure, P_e is the pressure at which pore compaction occurs, and P_s is the fully compacted pressure.

2.2. Nonlinear Yield Criterion. The mechanical properties and yield criterion for rock-like materials are always the concern of researchers in fields as mining science [30], geology [31], and rock engineering [32–34]. In the plastic range, to describe the confining pressure effect on yield strength for rock-like materials, the experimental data are smoothed and approximated according to the method first proposed by Lundborg [35], considering the similarities between concrete and rock in terms of mechanical response. For intact concrete, there is an initial tensile strength f_t and a cohesion strength τ_0. The local slope of the strength-pressure curve is called the internal friction coefficient μ; the shear strength reaches a constant τ_m at a sufficiently high-pressure state. The nonlinear yield criterion in a spherically symmetric Euler coordinate system is

$$\sigma_r - \sigma_\theta = \tau_0 + \frac{P}{1/\mu + (1/\tau_m - \tau_0)P}, \tag{2a}$$

$$P = \frac{(\sigma_r + 2\sigma_\theta)}{3}, \tag{2b}$$

where σ_r and σ_θ are the radial and hoop Cauchy stress components, which are taken as positive in compression. In summary, setting $\tau_0 = a_0$, $1/\mu = a_1$, and $1/(\tau_m - \tau_0) = a_2$, and then, Eq. (2a) can be expressed as $\sigma_r - \sigma_\theta = a_0 + P/(a_1 + a_2 P)$. a_0, a_1, and a_2 are constants which obtained by a series of triaxial compression test data.

3. Development of Dynamic Spherical Cavity Expansion Model

The cavity expansion generates an elastic-cracked-compacted response (Figure 1(a)) or elastic-compacted response (Figure 1(b)) which depends on the cavity expansion velocity V_r, where r is the radial Eulerian coordinate, c and c_1 are the boundary velocities, c_d is the dilatational velocity, and t is the time.

3.1. Compacted Region. The mass conservation and momentum conservation equations of the compressible medium in Euler coordinates are

$$\rho\left(\frac{\partial v}{\partial r} + \frac{2v}{r}\right) = -\left(\frac{\partial \rho}{\partial t} + v\frac{\partial \rho}{\partial r}\right), \tag{3a}$$

$$\frac{\partial \sigma_r}{\partial r} + \frac{2(\sigma_r - \sigma_\theta)}{r} = -\rho\left(\frac{\partial v}{\partial t} + v\frac{\partial v}{\partial r}\right), \tag{3b}$$

where r is the radial Eulerian coordinate and v is the particle velocity (outward is positive).

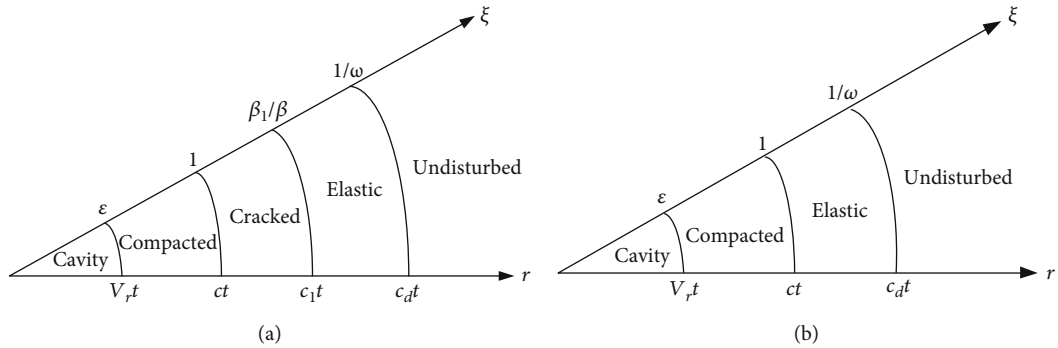

Figure 1: Two types of target responses: (a) elastic-cracked-compacted response and (b) elastic-compacted response.

By defining the following dimensionless variables and introducing similar transformations,

$$\xi = \frac{r}{ct},$$

$$U = \frac{v}{c},$$

$$\varepsilon = \frac{V_r}{c},$$

$$F = \frac{f_t}{f_c},$$

$$S = \frac{\sigma_r}{f_c},$$

$$T = \frac{P}{f_c},$$

$$\beta_1 = \frac{c_1}{c_p},$$

$$\beta = \frac{c}{c_p},$$

$$c_p = \sqrt{K/\rho_0}. \tag{4}$$

Transform Eq. (3) into the following dimensionless forms

$$\frac{dU}{d\xi} + 2\frac{U}{\xi} = f(T)(\xi - U)\frac{dT}{d\xi}, \tag{5a}$$

$$h(T)f_c\frac{dT}{d\xi} + 2\frac{g(T)}{\xi} = i(T)(\xi - U)\frac{dU}{d\xi}, \tag{5b}$$

where f_c and f_t are the static uniaxial compressive and tensile strength of concrete. $f(T)$, $g(T)$, $h(T)$, and $i(T)$ can be derived with Eqs. (1) and (2).

$$f(T) = \frac{3f_c(\alpha_0 - 1)(P_s - f_cT)^2}{(P_s - P_e)^3 + (\alpha_0 - 1)(P_s - f_cT)^3}, \tag{6a}$$

$$g(T) = a_0 + \frac{f_cT}{a_1 + a_2f_cT}, \tag{6b}$$

$$h(T) = 1 + \frac{2}{3}(a_1 + a_2f_cT) - \frac{2a_2f_cT}{3(a_1 + a_2f_cT)^2}, \tag{6c}$$

$$i(T) = \frac{\alpha_0\beta^2K}{1 + (\alpha_0 - 1)(P_s - f_cT)^3/(P_s - P_e)^3}. \tag{6d}$$

From Eq. (2), the dimensionless relation between the pressure T and radial stress S obeys

$$S = \frac{2}{3f_c}\left(a_0 + \frac{f_cT}{a_1 + a_2f_cT}\right) + T. \tag{7}$$

Eq. (5) is transformed by the Runge-Kutte method to evaluate it numerically.

$$\frac{dU}{d\xi} = \frac{2(\xi - U)f(T)g(T) + 2Uf_ch(T)}{\xi(\xi - U)^2f(T)i(T) - f_c\xi h(T)}, \tag{8a}$$

$$\frac{dT}{d\xi} = \frac{2g(T) + 2U(\xi - U)i(T)}{\xi(\xi - U)^2f(T)i(T) - f_c\xi h(T)}. \tag{8b}$$

When the Hugoniot jump condition is given, the initial values for U and T in Eq. (8) can be determined by the solutions in the cracked region (Figure 1(a)) or elastic region (Figure 1(b)) at $\xi = 1$. These two types of target responses are presented separately below.

3.2. Elastic-Cracked-Compacted Response. In the elastic region, the stress-strain relation is governed by Hooke's law.

$$\sigma_r = -\frac{E}{(1 + \nu)(1 - 2\nu)}\left[(1 - \nu)\frac{\partial u}{\partial r} + 2\nu\frac{u}{r}\right], \tag{9a}$$

$$\sigma_\theta = -\frac{E}{(1+\nu)(1-2\nu)}\left[\nu\frac{\partial u}{\partial r} + \frac{u}{r}\right], \tag{9b}$$

where u is the outward radial displacement (positive direction).

Considering that elastic deformation is very small, ignoring the convective term in Eq. (3b) [14, 22] and substituting Eq. (9) into Eq. (3b) obeys the wave equation

$$\frac{\partial^2 u}{\partial r^2} + \frac{2}{r}\frac{\partial u}{\partial r} - \frac{2u}{r^2} = \frac{1}{{c_d}^2}\frac{\partial^2 u}{\partial t^2}, \tag{10a}$$

$${c_d}^2 = \frac{E(1-\nu)}{(1+\nu)(1-2\nu)\rho_0}. \tag{10b}$$

By introducing a new dimensionless variable $u = u/ct$ and adopting the similarity transformation, Eq. (10a) can be expressed in another form.

$$\left(1-\omega^2\xi^2\right)\frac{d^2\bar{u}}{d\xi^2} + \frac{2}{\xi}\frac{d\bar{u}}{d\xi} - \frac{2}{\xi^2}\bar{u} = 0, \tag{11a}$$

$$\omega = \frac{c}{c_d} = \beta\sqrt{K(1+\nu)(1-2\nu)/(E(1-\nu))}. \tag{11b}$$

Integrating Eq. (11a) gives the following general solution.

$$\bar{u} = A_0\omega\xi - B_0\frac{1-3\omega^2\xi^2}{3\omega^2\xi^2}, \tag{12}$$

where A_0 and B_0 are the unknown integral constants, which can be obtained using the following boundary conditions.

$$\bar{u}\frac{\xi=1}{\omega} = 0, \tag{13a}$$

$$\sigma_\theta\frac{\xi=\beta_1}{\beta} = -f_t. \tag{13b}$$

Combining Eqs. (12) and (13) yields

$$B_0 = -\frac{3}{2}A_0, \tag{14a}$$

$$A_0 = \frac{2f_t}{E}\cdot\frac{\omega^2{\beta_1}^3(1+\nu)(1-2\nu)}{\left[2\omega^3{\beta_1}^3(1+\nu)+\beta^3(1-2\nu)-3\omega^2\beta{\beta_1}^2\right]}. \tag{14b}$$

Furthermore, the relation between the particle velocity and radial displacement is

$$\nu\left(1-\frac{\partial u}{\partial r}\right) = \frac{\partial u}{\partial t}. \tag{15}$$

Substituting Eq. (12) into Eq. (15) and considering the strain in elastic region is small, Eq. (15) can be revised as

$$U = \bar{u} - \xi\frac{du}{d\xi}. \tag{16}$$

Using Eqs. (9b), (12), (13), and (16), the dimensionless radial stress S_1 and particle velocity U_1 in the elastic region at $\xi = \beta_1/\beta$ are derived as

$$S_1 = 2F\left[\frac{(1-2\nu)+3\nu(\gamma\beta_1)^2-(1+\nu)(\gamma\beta_1)^3}{1-2\nu-3(\gamma\beta_1)^2+2(1+\nu)(\gamma\beta_1)^3}\right], \tag{17a}$$

$$\beta U_1 = \frac{3f_t\beta_1(1+\nu)(1-2\nu)}{E}\left[\frac{1-(\gamma\beta_1)^2}{1-2\nu-3(\gamma\beta_1)^2+2(1+\nu)(\gamma\beta_1)^3}\right], \tag{17b}$$

$$\gamma^2 = \left(\frac{c_p}{c_d}\right)^2 = \frac{1+\nu}{3(1-\nu)}. \tag{17c}$$

Using the Hugoniot jump conditions in the cracked region at $\xi = \beta_1/\beta$, the dimensionless radial stress S_2 and particle velocity U_2 can be obtained, i.e.,

$$S_2 = S_1 + \frac{2F(\beta_1-\beta U_1)^2}{3-(\beta_1-\beta U_1)^2}, \tag{18a}$$

$$\beta U_2 = \beta U_1 + \frac{(2f_t/K)(\beta_1-\beta U_1)}{3-(\beta_1-\beta U_1)^2}. \tag{18b}$$

Moreover, concrete is considered to be a linear compressible material in the cracked region when $\sigma_\theta = 0$, and then, the general solutions in the cracked region can be described as

$$S(\xi) = \frac{C_0}{\beta\xi} + D_0\left[1+\frac{3}{(\beta\xi)^2}\right], \tag{19a}$$

$$U(\xi) = \frac{-f_c}{2K\beta}\left[\frac{C_0}{3} + \frac{C_0}{(\beta\xi)^2} + \frac{4D_0}{\beta\xi}\right], \tag{19b}$$

where C_0 and D_0 are the integral constants. Based on the boundary conditions in Eq. (18), it can be determined as follows:

$$C_0 = \frac{-6{\beta_1}^2\left[2\beta_1 f_c S_2 + K\left({\beta_1}^2+3\right)(\beta U_2)\right]}{f_c\left({\beta_1}^2-3\right)^2}, \tag{20a}$$

$$D_0 = \frac{\beta_1{}^2\left[f_c S_2\left(\beta_1{}^2+3\right)+6\beta_1 K(\beta U_2)\right]}{f_c\left(\beta_1{}^2-3\right)^2}. \tag{20b}$$

The above-mentioned nonlinear yield criterion is satisfied in the cracked region at $\xi = \beta_1/\beta$; thus,

$$\sigma_r = a_0 + \frac{\sigma_r/3}{a_1 + a_2\sigma_r/3}, \tag{21a}$$

$$\frac{\sigma_r}{f_c} = \frac{C_0}{\beta} + D_0\frac{1+3}{\beta^2}. \tag{21b}$$

By using Eq. (21), β can be expressed as

$$\beta = \frac{C_0 + \sqrt{C_0{}^2 + 12D_0(E_0 - D_0)}}{2(E_0 - D_0)}, \tag{22a}$$

$$E_0 = \frac{-3a_1 + a_0a_2 + 1 + \sqrt{9a_1{}^2 + a_0{}^2a_2{}^2 + 2a_0a_2 + 6a_0a_1a_2 - 6a_1 + 1}}{2a_2f_c}. \tag{22b}$$

In the cracked region at $\xi = 1$, the dimensionless radial stress S_3, pressure T_3, and particle velocity U_3 can be obtained as

$$\begin{aligned} S_3 &= E_0, \\ T_3 &= \frac{E_0}{3}, \\ U_3 &= -\frac{f_cC_0\left(\beta^2+3\right)}{6K\beta^3} - \frac{2f_cD_0}{K\beta^2}. \end{aligned} \tag{23}$$

3.3. Elastic-Compacted Response. The target response can be simplified to the elastic-compacted type when $c > c_1$. The solution for u is consistent with Eq. (12), while the integral constants should be obtained from the following boundary conditions.

$$\bar{u}\frac{\xi = 1}{\omega} = 0, \tag{24a}$$

$$\sigma_r(\xi = 1) - \sigma_\theta(\xi = 1) = a_0 + \frac{\sigma_r(\xi = 1) + 2\sigma_\theta(\xi = 1)}{3a_1 + a_2(\sigma_r(\xi = 1) + 2\sigma_\theta(\xi = 1))}. \tag{24b}$$

Substituting the boundary conditions into the displacement solution in Eq. (12), we have

$$B_0{}' = -\frac{3}{2}A_0{}', \tag{25a}$$

$$A_0{}' = \frac{-y_0 + \sqrt{y_0{}^2 - 4x_0z_0}}{2x_0}, \tag{25b}$$

where x_0, y_0, and z_0 are constants, which can be written as

$$x_0 = 3a_2E^2\left(1-\omega^2\right), \tag{26a}$$

$$y_0 = 3a_1E(1-2\nu)(1+\omega) - 2E(a_0a_2+1)(1+\nu)\omega^2, \tag{26b}$$

$$z_0 = \frac{2a_0a_1\omega^2(1+\nu)(1-2\nu)}{(\omega-1)}. \tag{26c}$$

In the elastic region at the elastic-compacted interface ($\xi = 1$), using Eqs. (9), (12), (24), (25) and (26), then S_3, T_3, and U_3 are obtained.

$$\begin{aligned} S_3 &= \frac{EA_0{}'\left[(1+\nu)\omega^3 - 3\nu\omega^2 + 2\nu - 1\right]}{f_c(1+\nu)(2\nu-1)\omega^2}, \\ T_3 &= \frac{EA_0{}'(\omega-1)}{f_c(2\nu-1)}, \\ U_3 &= \frac{3}{2}\left(\frac{1}{\omega^2} - 1\right)A_0{}'. \end{aligned} \tag{27}$$

3.4. Hugoniot Jump Conditions. To solve the dimensionless conservation equation in Eq. (8) still requires a dimensionless pressure and particle velocity in the compacted region at the cracked-compacted interface or elastic-compacted interface; it can be obtained with the Hugoniot jump conditions. Noticing that subscript 3 represents the variable in the cracked or elastic region at $\xi = 1$, and subscript 4 represents the variable in the compacted region at $\xi = 1$. The concrete is treated as a linear compressible material in the elastic or cracked regions at $\xi = 1$, i.e.,

$$T_3f_c = K\left(1 - \frac{\rho_0}{\rho_3}\right). \tag{28}$$

The P-α EOS is used for the compacted region; therefore,

$$\rho_4 = \frac{\alpha_0\rho_0}{1 + (\alpha_0 - 1)(P_s - T_4f_c)^3/(P_s - P_e)^3}. \tag{29}$$

For the dimensionless Hugoniot jump conditions, it follows that

$$U_4 = 1 + \left(\frac{\rho_3}{\rho_4}\right)(U_3 - 1), \tag{30a}$$

$$S_4 = \frac{S_3 + \rho_3c^2(1-U_3)(U_4-U_3)}{f_c}. \tag{30b}$$

By solving Eqs. (7) and (28)-(30), S_4, T_4, and U_4 in the compacted region at $\xi = 1$ are obtained, and then used as the initial values of the dimensionless conservation equation in Eq. (8).

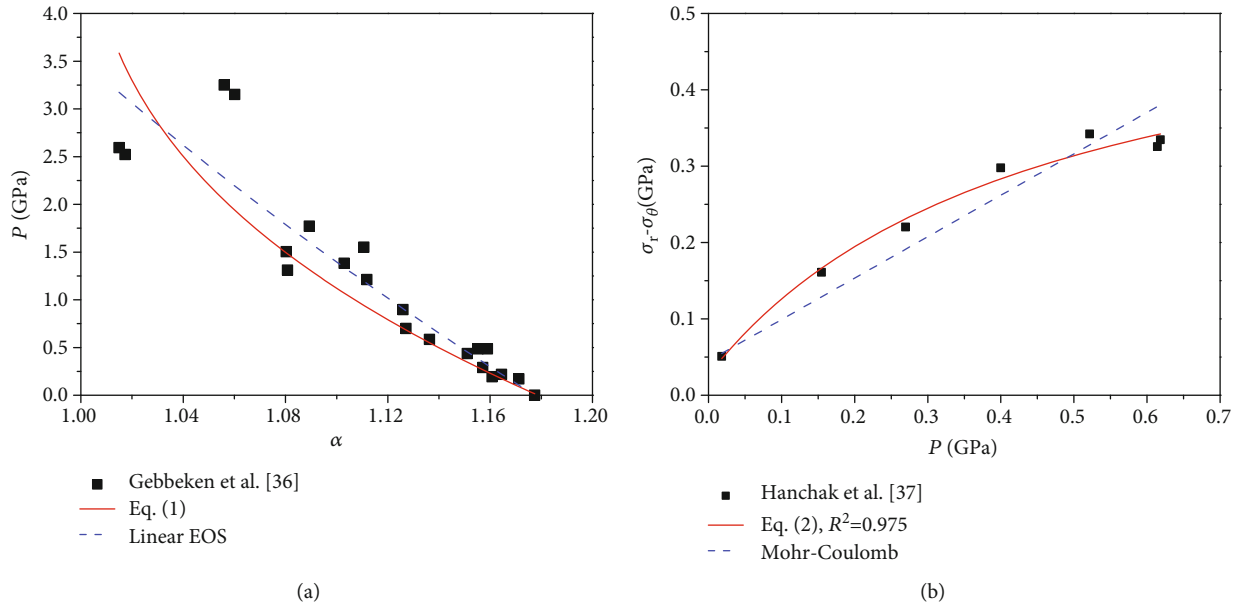

Figure 2: Test data and proposed constitutive laws for 51 MPa concrete: (a) EOS and (b) yield criterion.

To establish the penetration model, it is necessary to clarify the relationship between σ_r and V_r. The cavity expansion resistance of concrete is generally expressed as the following three components [15], i.e.,

$$\frac{\sigma_r}{f_c} = A + B\left(\frac{V_r}{\sqrt{f_c/\rho_0}}\right) + C\left(\frac{V_r}{\sqrt{f_c/\rho_0}}\right)^2, \tag{31}$$

where A, B, and C denote the dimensionless resistance constants.

Here, we can choose concrete with uniaxial compressive strength of 51 MPa to analyze the proposed dynamic cavity expansion model in detail. For the EOS, referring to the isotropic compression data of 51.2 MPa concrete [36], the fitting results using Eq. (1a) are shown in Figure 2(a). The initial and fully compacted densities of the concrete are 2350 kg/m^3 and 2767 kg/m^3, respectively. Using the P-α EOS with $\alpha_0 = 1.177$, $P_e = 17$ MPa, and $P_s = 6370$ MPa gives satisfying agreement with the test data. For the relation between the shear strength and pressure, the existing literature lacks the triaxial data of 51 MPa concrete, so the 48 MPa concrete triaxial data from Hanchak et al. [37] is used instead, and the fitted results by Eq. (2) are presented in Figure 2(b). Obviously, the nonlinear yield criterion presented in this paper can effectively reproduce the test data (adjusted $R^2 = 0.975$) with $a_0 = 26.67$ MPa, $a_1 = 0.82$, and $a_2 = 1.84 \times 10^{-3}$ MPa^{-1}. In contrast, the Mohr-Coulomb yield criterion shows poor agreement with the experimental data. The constitutive parameters for 51 MPa concrete are summarized as follows:

$\rho_0 = 2350$ kg/m^3, $\rho_s = 2767$ kg/m^3, $\alpha_0 = 1.177$, $P_e = 17$ MPa, and $P_s = 6370$ MPa

$a_0 = 26.67$ MPa, $a_1 = 0.82$, and $a_2 = 1.84 \times 10^{-3}$ MPa^{-1}

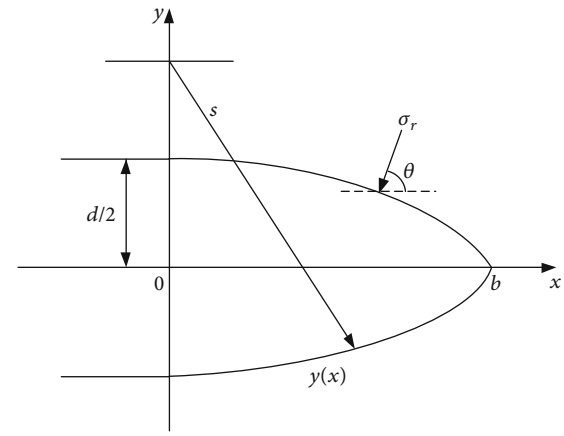

Figure 3: Diagram of an ogive-nosed projectile.

4. Model Validation

4.1. Deep Penetration Analysis of an Ogive-Nosed Projectile. The axial resistance acting on the projectile nose is given by the following expression.

$$dF_x = \sigma_r \cos\theta dS. \tag{32}$$

If the tangential friction stress is neglected [38], the final axial penetration resistance F_x can be expressed as

$$F_x = m\frac{dV}{dt} = \frac{\pi d^2}{4}\left(AN_0 f_c + BN_1\sqrt{\rho_0 f_c}V + CN_2\rho_0 V^2\right), \tag{33}$$

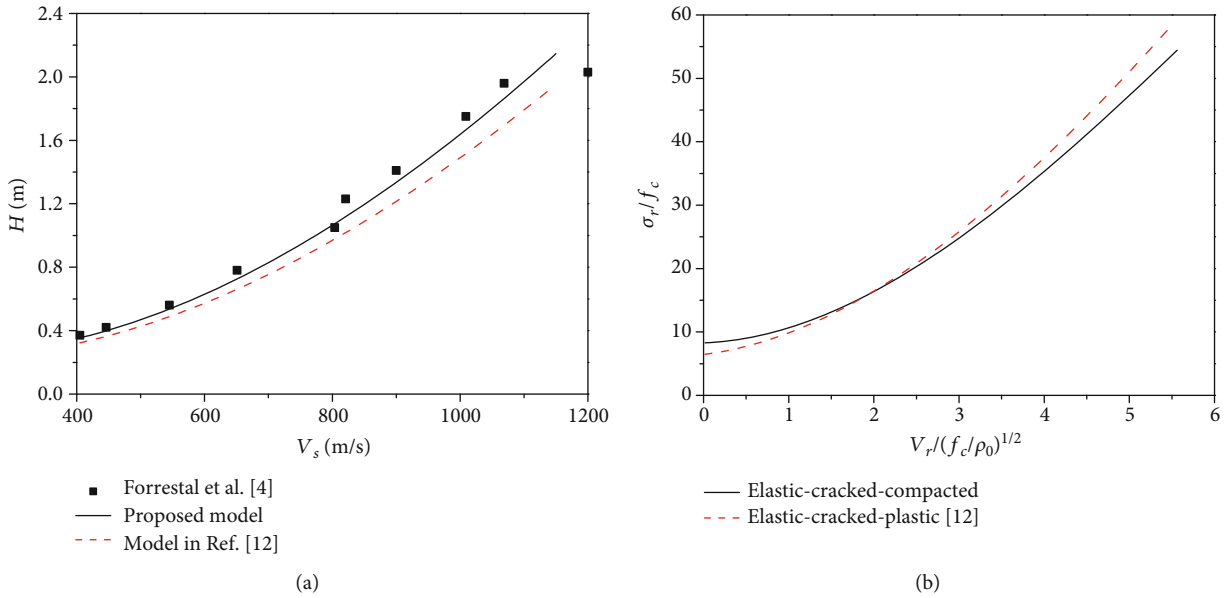

Figure 4: Model verification for 51 MPa concrete: (a) comparison of predicted and experimental DOP and (b) cavity surface radial stress calculation results of the elastic-cracked-compacted and elastic-cracked-plastic model.

where N_0, N_1, and N_2 are the nondimensional quantities related to the projectile nose shape, i.e.,

$$\begin{aligned} N_0 &= 1, \\ N_1 &= \frac{8}{d^2}\int_0^b \frac{yy'^2}{\sqrt{1+y'^2}}dx, \\ N_2 &= \frac{8}{d^2}\int_0^b \frac{yy'^3}{1+y'^2}dx. \end{aligned} \tag{34}$$

As Figure 3 shows, for ogive-nosed projectile, it follows that

$$\begin{aligned} N_0 &= 1, \\ N_1(\psi) &= \frac{(4\psi-1)^{3/2}}{3\psi} + \frac{(2\psi-1)^2(4\psi-1)^{1/2}}{2\psi} \\ &\quad - \psi(2\psi-1)(\pi-2\theta_0), \\ N_2(\psi) &= \frac{8\psi-1}{24\psi^2}, \theta_0 = \sin^{-1}\left(\frac{2\psi-1}{2\psi}\right), \end{aligned} \tag{35}$$

where $\psi = s/d$ and s is defined in Figure 3. The final DOP H can be derived by integrating Eq. (33).

$$\begin{aligned} H = {} & \frac{m}{2\pi a^2 C N_2 \rho_0}\left\{\ln\left[1+\frac{BN_1}{A}\left(\frac{\rho_0}{f_c}\right)^{1/2}V_1 + \frac{CN_2\rho_0}{Af_c}V_1^2\right]\right. \\ & \left. + \frac{2BN_1}{D}\left[\arctan\left(\frac{BN_1}{D}\right) - \arctan\left(\frac{BN_1+2CN_2(\rho_0/f_c)^{1/2}}{D}\right)\right]\right\} \\ & + 4a, \quad H > 4a, \end{aligned} \tag{36}$$

where $D = \left[4ACN_2 - (BN_1)^2\right]^{1/2}$, and V_1 is projectile velocity at penetration depth $4a$ which was obtained from

$$\left[\frac{m}{4\pi a^3 f_c} + \frac{CN_2}{(f_c/\rho_0)}\right]\cdot V_1^2 + \frac{BN_1}{(f_c/\rho_0)^{1/2}}\cdot V_1 + \left[A - \frac{mV_s^2}{4\pi a^3 f_c}\right] = 0. \tag{37}$$

For Eqs. (35)-(37), m is the projectile mass, $d = 2a$ is the shank diameter, and V_s is the initial striking velocity.

4.2. Comparisons with the Penetration Test Data. First, the proposed model is verified based on the test data of projectile penetration into 51 MPa concrete [4]. The *P-α* EOS and nonlinear yield criterion shown in Figure 2 are employed. Then, the predicted and experimental DOP are compared in Figure 4(a). It shows that the proposed model gives better agreement than the model in Ref. [12], especially at relatively high-impact velocities. Figure 4(b) illustrates the cavity surface radial stress versus the cavity expansion velocity of the elastic-cracked-compacted and elastic-cracked-plastic [12] models. Correspondingly, the cavity expansion resistance function parameters calibrated as $A = 7.4$, $B = 2.5$, and $C = 1.1$ and $A = 5.8$, $B = 3.0$, and $C = 1.2$, respectively. When $V_r/(f_c/\rho_0)^{1/2} < 1.8$, the cavity surface radial stress σ_r calculated by the elastic-cracked-compacted model is slightly larger than that of the elastic-cracked-plastic model. When $V_r/(f_c/\rho_0)^{1/2} > 1.8$, the σ_r in the elastic-cracked-compacted model is smaller than the elastic-cracked-plastic model, and the difference between the two models becomes greater with increasing of the cavity expansion velocity. This also explains why the elastic-cracked-plastic model cannot effectively predict the penetration depth under relatively high-impact velocities.

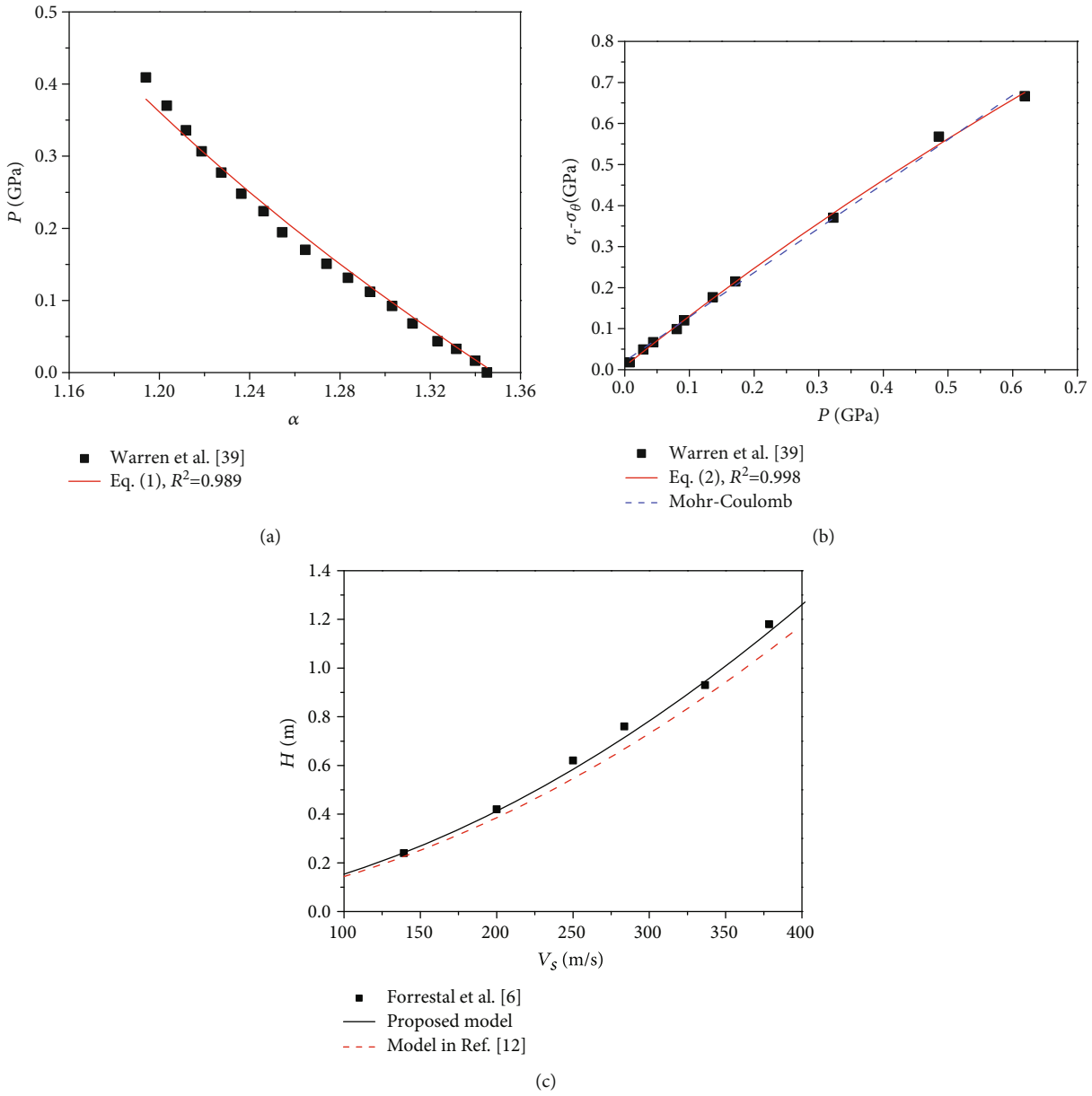

Figure 5: Comparison of theoretical model and test data for 23 MPa concrete: (a) EOS, (b) yield criterion, and (c) DOP.

For 23 MPa concrete, the test results [39] with P-α EOS and nonlinear yield criterion by data fitting are plotted in Figures 5(a) and 5(b), where $\rho_0 = 1.97\,\text{g/cm}^3$, $\alpha_0 = 1.345$, $P_e = 7.6$ MPa, $P_s = 2138$ MPa, $a_0 = 8.49$ MPa, $a_1 = 0.79$, and $a_2 = 2.12 \times 10^{-4}\,\text{MPa}^{-1}$. As Figure 5(c) shows, the predicted DOP by the proposed model is in better agreement with the test data than the classic model in Ref. [12].

For 36 MPa concrete, using the hydrostatic pressure-shear strength test data from Ref. [3], the fitting results with nonlinear least squares are plotted in Figure 6(a). For the EOS, since the pressure-porosity data of 36 MPa concrete are absent, the concrete exhibits similar compaction characteristics when the strength is very close. Therefore, using the EOS parameters from 35 MPa [40] concrete seems reasonable. The constitutive parameters for 36 MPa concrete are summarized as follows: $\rho_0 = 2.31\,\text{g/cm}^3$, $\alpha_0 = 1.19$, $P_e = 23.3$ MPa, $P_s = 6000$ MPa, $a_0 = 22.89$ MPa, $a_1 = 0.72$, and $a_2 = 2.17 \times 10^{-3}\,\text{MPa}^{-1}$. Figure 6(b) demonstrates that the proposed model provides better predictions than the classic model, and it can be inferred that the underestimation DOP of the classic model mainly comes from the use of the linear constitutive relations.

4.3. Further Discussions. To obtain the parameters of the nonlinear constitutive in Eqs. (1) and (2), i.e., P_e, P_s, a_0, a_1, and a_2, the pressure-porosity data from flyer-plate impact tests and the hydrostatic pressure-shear strength data from triaxial compression tests are needed. However, most DOP tests lack the necessary data required for analysis and calculation models. Under this circumstance, the parameters of a_0, a_1, and a_2 are taken from the method proposed by

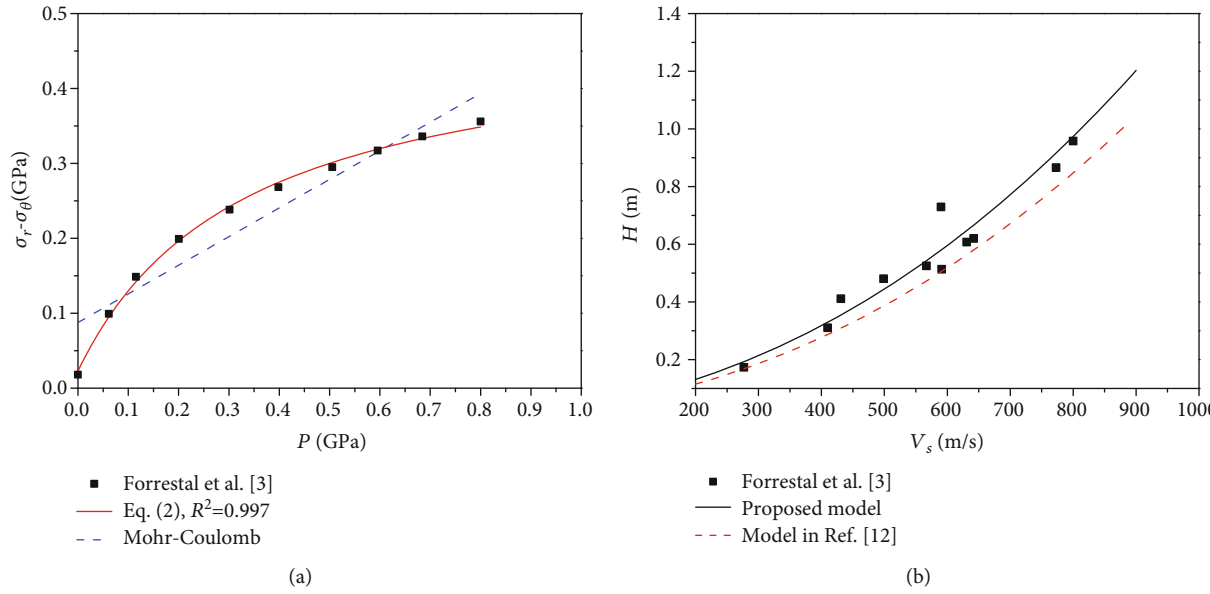

Figure 6: Comparison of theoretical model and test data for 36 MPa concrete: (a) yield criterion and (b) DOP.

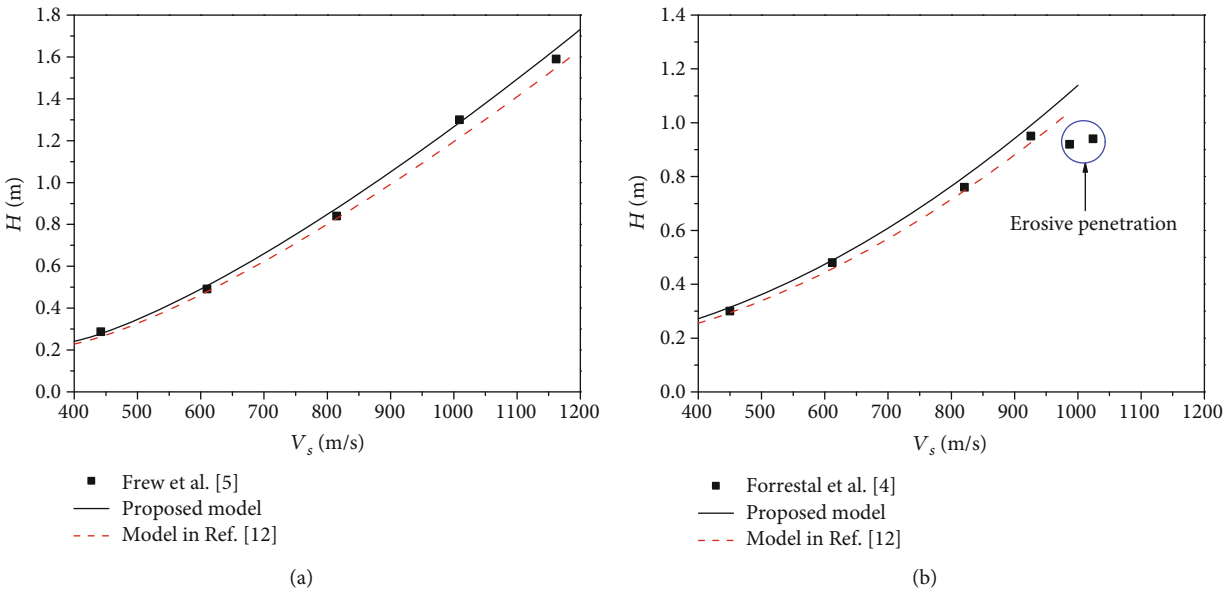

Figure 7: Comparison of predicted and experimental DOP for (a) 58.4 MPa and (b) 62.8 MPa concrete.

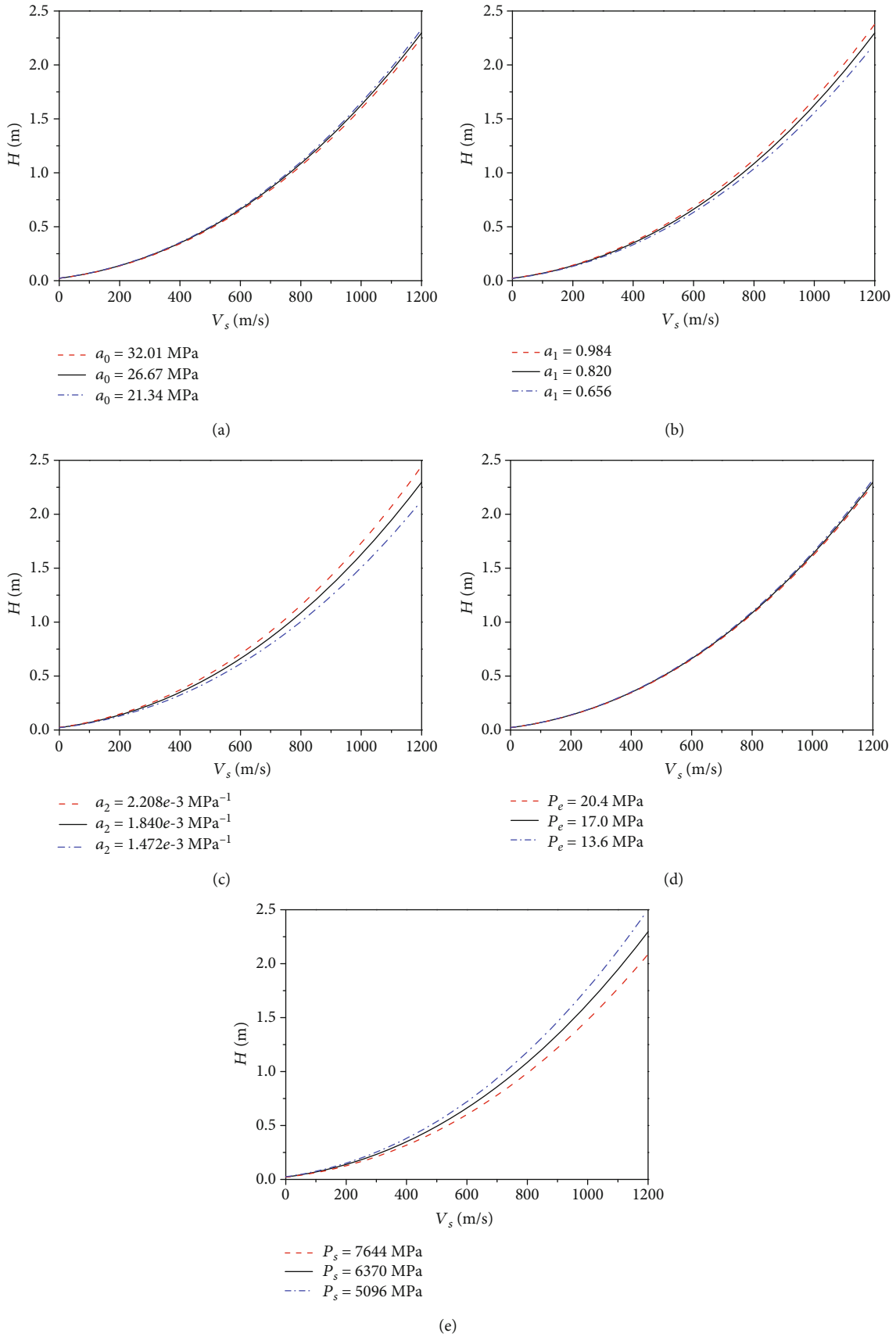

Figure 8: Influence of the target material parameters on the DOP (a) a_0, (b) a_1, (c) a_2, (d) P_e, and (e) P_s.

Markovich et al. [41] as well as the value of P_e suggested by Holmquist et al. [42]. The default values of P_s for 35 MPa and 140 MPa concrete are both equal to 6 GPa in AUTODYN version 6.1 [43]. Here, the compacted pressure P_s is also recommended to be 6 GPa for $f_c = 58.4$ MPa and $f_c = 62.8$ MPa concrete. Thus, the constitutive parameters of normal concrete are summarized as follows:

$$a_0 = 2.442 f_c^{0.4369},$$

$$a_1 = 1.084 f_c^{-0.2463},$$

$$a_1 = 0.03276 f_c^{-0.6416}, \tag{38a}$$

$$P_e = \frac{f_c}{3},$$

$$P_s = 6\,\text{GPa}, \tag{38b}$$

where f_c is measured in MPa.

Figure 7 gives the experimental data from Refs. [4, 5] and the predicted DOP by Eq. (36), where the parameters of the P-α EOS and nonlinear yield criterion are given in Eq. (38). Most of the predictions show reasonable agreement with the test data except for two points, which are marked by a circle in Figure 7(b). The overestimations of the DOP for these two data points may lie in that if the striking velocity exceeds 987 m/s, the projectile mass loss will aggravate, and the mass abrasive penetration regime occurs.

5. The Influence of the Concrete Constitutive Parameters on the DOP

Taking 51 MPa concrete target as an example, the influences of the concrete constitutive parameters on the DOP are discussed below. Figure 8 illustrates the effects of one specific variable on the DOP while maintains other variables to be same. During the theoretical analysis, $\rho_0 = 2.35\,\text{g/cm}^3$ and $\alpha_0 = 1.177$.

From Figure 8(a), it is observed that if a_0 increases by 50%, the DOP decreases by 3.8%, 3.4%, and 3.2% when the striking velocity is 400 m/s, 800 m/s, and 1200 m/s, respectively. Obviously, the DOP is relatively less affected by the cohesion in different velocity ranges.

As Figure 8(b) shows, if a_1 increases by 50%, the DOP increases by 6.8%, 7.1%, and 7.2% when the striking velocity is 400 m/s, 800 m/s, and 1200 m/s, respectively. In this respect, the coefficient of internal friction μ has a considerable influence on the DOP.

As can be seen in Figure 8(c), if a_2 increases by 50%, the DOP increases by 7%, 10.2%, and 12.5% when the striking velocity is 400 m/s, 800 m/s, and 1200 m/s, respectively. Therefore, we believe the von Mises plastic limit τ_m has a substantial influence on the DOP.

As is observed in Figure 8(d), if P_e increases by 50%, the DOP decreases by 2.5%, 1.9%, and 1.6% when the striking velocity is 400 m/s, 800 m/s, and 1200 m/s, respectively. In general, the influence of the elastic limit on the DOP decreases with increasing striking velocity and is negligibly small at high striking velocities.

From Figure 8(e), if P_s increases by 50%, the DOP decreases by 6.8%, 12.0%, and 16.6% when the striking velocity is 400 m/s, 800 m/s, and 1200 m/s, respectively. It is observed that the influence of compacted pressure on the DOP increases with increasing striking velocities. For lower impact velocities, the effect of P_s on the DOP is relatively small, and for higher striking velocities, it may become considerably large.

6. Conclusions

(1) The P-α EOS and nonlinear yield criterion are employed to characterize the plastic mechanical response of concrete under impact loading. Then, an improved dynamic spherical cavity expansion model considering the concrete compressibility and nonlinear constitutive relations is established

(2) A penetration model to predict the DOP is obtained, and the proposed model seems to better predict the available test results compared to the classic model derived from the linear EOS and yield criterion

(3) The parameters a_2 and P_s have a great influence on the DOP while the internal friction coefficient μ has a considerable influence on the DOP. In contrast, a_1 and P_e have a relatively small influence on the DOP and are weakly dependent on the striking velocities

Data Availability

The figures presenting the data analysis were all drawn in Origin 8.0. The formula derivation process and theoretical calculation data files used to support the findings of this study are available from the corresponding author upon request.

Conflicts of Interest

The authors declare that they have no conflicts of interest.

Acknowledgments

This research is supported by the National Natural Science Foundation of China (Grant Nos. 12002171 and 42002266).

References

[1] H. Xu and H. M. Wen, "A computational constitutive model for concrete subjected to dynamic loadings," *International Journal of Impact Engineering*, vol. 91, pp. 116–125, 2016.

[2] Q. M. Li, S. R. Reid, H. M. Wen, and A. R. Telford, "Local impact effects of hard missiles on concrete targets," *International Journal of Impact Engineering*, vol. 32, no. 1-4, pp. 224–284, 2005.

[3] M. J. Forrestal, J. D. Cargile, and D. Y. Tzou, *Penetration of Concrete Targets*, Sandia National Labs., Albuquerque, NM(United States), 1993.

[4] M. J. Forrestal, D. J. Frew, S. J. Hanchak, and N. S. Brar, "Penetration of grout and concrete targets with ogive-nose steel projectiles," *International Journal of Impact Engineering*, vol. 18, no. 5, pp. 465–476, 1996.

[5] D. J. Frew, S. J. Hanchak, M. L. Green, and M. J. Forrestal, "Penetration of concrete targets with ogive-nose steel rods," *International Journal of Impact Engineering*, vol. 21, no. 6, pp. 489–497, 1998.

[6] M. J. Forrestal, D. J. Frew, J. P. Hickerson, and T. A. Rohwer, "Penetration of concrete targets with deceleration-time measurements," *International Journal of Impact Engineering*, vol. 28, no. 5, pp. 479–497, 2003.

[7] M. Unosson and L. Nilsson, "Projectile penetration and perforation of high performance concrete: experimental results and macroscopic modelling," *International Journal of Impact Engineering*, vol. 32, no. 7, pp. 1068–1085, 2006.

[8] A. Dawson, S. Bless, S. Levinson, B. Pedersen, and S. Satapathy, "Hypervelocity penetration of concrete," *International Journal of Impact Engineering*, vol. 35, no. 12, pp. 1484–1489, 2008.

[9] R. F. Bishop, R. Hill, and N. F. Mott, "The theory of indentation and hardness tests," *Proceedings of the Physical Society*, vol. 57, no. 3, pp. 147–159, 1945.

[10] R. Hill, *A Theory of Earth Movement Near a Deep Underground Explosion. Memo No.21-48*, Armament Research Establishment, Front Halstead, Kent, UK, 1948.

[11] V. K. Luk and M. J. Forrestal, "Penetration into semi-infinite reinforced-concrete targets with spherical and ogival nose projectiles," *International Journal of Impact Engineering*, vol. 6, no. 4, pp. 291–301, 1987.

[12] M. J. Forrestal and D. Y. Tzou, "A spherical cavity-expansion penetration model for concrete targets," *International Journal of Solids and Structures*, vol. 34, no. 31-32, pp. 4127–4146, 1997.

[13] Y. Xu, L. M. Keer, and V. K. Luk, "Elastic-cracked model for penetration into unreinforced concrete targets with ogival nose projectiles," *International Journal of Solids and Structures*, vol. 34, no. 12, pp. 1479–1491, 1997.

[14] T. He, H. M. Wen, and X. J. Guo, "A spherical cavity expansion model for penetration of ogival-nosed projectiles into concrete targets with shear-dilatancy," *Acta Mechanica Sinica*, vol. 27, no. 6, pp. 1001–1012, 2011.

[15] J. Feng, W. Li, X. Wang, M. Song, H. Ren, and W. Li, "Dynamic spherical cavity expansion analysis of rate-dependent concrete material with scale effect," *International Journal of Impact Engineering*, vol. 84, pp. 24–37, 2015.

[16] X. Z. Kong, H. Wu, Q. Fang, and Y. Peng, "Rigid and eroding projectile penetration into concrete targets based on an extended dynamic cavity expansion model," *International Journal of Impact Engineering*, vol. 100, pp. 13–22, 2017.

[17] X. Z. Kong, H. Wu, Q. Fang, and G. M. Ren, "Analyses of rigid projectile penetration into UHPCC target based on an improved dynamic cavity expansion model," *Construction and Building Materials*, vol. 126, pp. 759–767, 2016.

[18] M. J. Forrestal, D. B. Longcope, and F. R. Norwood, "A model to estimate forces on conical penetrators into dry porous rock," *Journal of Applied Mechanics*, vol. 48, no. 1, pp. 25–29, 1981.

[19] M. J. Forrestal, "Penetration into dry porous rock," *International Journal of Solids and Structures*, vol. 22, no. 12, pp. 1485–1500, 1986.

[20] T. L. Warren, S. J. Hanchak, and K. L. Poormon, "Penetration of limestone targets by ogive-nosed VAR 4340steel projectiles at oblique angles: experiments and simulations," *International Journal of Impact Engineering*, vol. 30, no. 10, pp. 1307–1331, 2004.

[21] M. J. Forrestal and D. B. Longcope, "Target strength of ceramic materials for high-velocity penetration," *Journal of Applied Physics*, vol. 67, no. 8, pp. 3669–3672, 1990.

[22] S. Satapathy, "Dynamic spherical cavity expansion in brittle ceramics," *International Journal of Solids and Structures*, vol. 38, no. 32-33, pp. 5833–5845, 2001.

[23] C. Shi, M. Wang, J. Li, and M. Li, "A model of depth calculation for projectile penetration into dry sand and comparison with experiments," *International Journal of Impact Engineering*, vol. 73, pp. 112–122, 2014.

[24] C. Shi, M. Wang, K. Zhang, Y. Cheng, and X. Zhang, "Semi-analytical model for rigid and erosive long rods penetration into sand with consideration of compressibility," *International Journal of Impact Engineering*, vol. 83, pp. 1–10, 2015.

[25] M. J. Forrestal and V. K. Luk, "Penetration into soil targets," *International Journal of Impact Engineering*, vol. 12, no. 3, pp. 427–444, 1992.

[26] M. J. Forrestal, K. Okajima, and V. K. Luk, "Penetration of 6061-T651 aluminum targets with rigid long rods," *Journal of Applied Mechanics*, vol. 55, no. 4, pp. 755–760, 1988.

[27] M. J. Forrestal, D. Y. Tzou, E. Askari, and D. B. Longcope, "Penetration into ductile metal targets with rigid spherical-nose rods," *International Journal of Impact Engineering*, vol. 16, no. 5-6, pp. 699–710, 1995.

[28] L. H. Han, J. A. Elliott, A. C. Bentham, A. Mills, G. E. Amidon, and B. C. Hancock, "A modified Drucker-Prager Cap model for die compaction simulation of pharmaceutical powders," *International Journal of Solids and Structures*, vol. 45, no. 10, pp. 3088–3106, 2008.

[29] W. Herrmann, "Constitutive equation for the dynamic compaction of ductile porous materials," *Journal of Applied Physics*, vol. 40, no. 6, pp. 2490–2499, 1969.

[30] X. Wang, C. Liu, S. Chen, L. Chen, K. Li, and N. Liu, "Impact of coal sector's de-capacity policy on coal price," *Applied Energy*, vol. 265, article 114802, 2020.

[31] C. Zhu, M. He, M. Karakus, X. Cui, and Z. Tao, "Investigating toppling failure mechanism of anti-dip layered slope due to excavation by physical modelling," *Rock Mechanics and Rock Engineering*, vol. 53, no. 11, pp. 5029–5050, 2020.

[32] C. Zhu, X. Xu, W. Liu et al., "Softening damage analysis of gypsum rock with water immersion time based on laboratory experiment," *IEEE Access*, vol. 7, pp. 125575–125585, 2019.

[33] H. Pan, D. Yin, N. Jiang, and Z. Xia, "Crack initiation behaviors of granite specimens containing crossing-double- flaws with different lengths under uniaxial loading," *Advances in Civil Engineering*, vol. 2020, Article ID 8871335, 13 pages, 2020.

[34] Q. Meng, H. Wang, M. Cai, W. Xu, X. Zhuang, and T. Rabczuk, "Three-dimensional mesoscale computational modeling of soil-rock mixtures with concave particles," *Engineering Geology*, vol. 277, article 105802, 2020.

[35] N. Lundborg, "Strength of rock-like materials," *International Journal of Rock Mechanics and Mining Sciences*, vol. 5, no. 5, pp. 427–454, 1968.

[36] N. Gebbeken, S. Greulich, and A. Pietzsch, "Hugoniot properties for concrete determined by full-scale detonation experiments and flyer-plate-impact tests," *International Journal of Impact Engineering*, vol. 32, no. 12, pp. 2017–2031, 2006.

[37] S. J. Hanchak, M. J. Forrestal, E. R. Young, and J. Q. Ehrgott, "Perforation of concrete slabs with 48 MPa (7 ksi) and 140 MPa (20 ksi) unconfined compressive strengths," *International Journal of Impact Engineering*, vol. 12, no. 1, pp. 1–7, 1992.

[38] X. W. Chen and Q. M. Li, "Deep penetration of a non-deformable projectile with different geometrical characteristics," *International Journal of Impact Engineering*, vol. 27, no. 6, pp. 619–637, 2002.

[39] T. L. Warren, A. F. Fossum, and D. J. Frew, "Penetration into low strength (23 MPa) concrete: target characterization and simulations," *International Journal of Impact Engineering*, vol. 30, no. 5, pp. 477–503, 2004.

[40] Z. Tu and Y. Lu, "Evaluation of typical concrete material models used in hydrocodes for high dynamic response simulations," *International Journal of Impact Engineering*, vol. 36, no. 1, pp. 132–146, 2009.

[41] N. Markovich, E. Kochavi, and G. Ben-Dor, "An improved calibration of the concrete damage model," *Finite Elements in Analysis and Design*, vol. 47, no. 11, pp. 1280–1290, 2011.

[42] T. J. Holmquist, G. R. Johnson, and W. H. Cook, "A computational constitutive model for concrete subjected to large strains, high strain rates, and high pressures," in *Proceedings of the 14th International Symposium on Ballistics*, pp. 591–600, Quebec, Canada, 1993.

[43] "AUTODYN v6.1 user manual," Century Dynamics, Inc., 2005.